The Image Navigation Cloud Mask for the Multiangle Imaging Spectroradiometer (MISR)

LARRY DI GIROLAMO AND ROGER DAVIES

Department of Atmospheric and Oceanic Sciences, McGill University, Montreal, Canada

(Manuscript received 26 July 1994, in final form 18 May 1995)

ABSTRACT

The authors have developed a cloud mask technique that may be applied to the efficient selection of "clear enough" scenes for image navigation. While the mask can be applied generally, the motivation for its development comes from its intended use on Multiangle Imaging Spectroradiometer (MISR) imagery. The difficulties in detecting clouds in the presence of land–water boundaries when using prenavigated imagery is overcome by using a simple two-step direct threshold technique. The two steps involve the thresholding of two observables derived for each pixel. The first is a 0.86-μm reflectance. The second is a new observable, $D = |\mathrm{NDVI}|^b R_1^{-2}$, where $\mathrm{NDVI} = (R_2 - R_1)(R_2 + R_1)^{-1}$, R_2 is the 0.86-μm reflectance, R_1 is the 0.67-μm reflectance, and b is chosen so as to maximize the separation between clear and cloudy pixels. The success of the cloud mask is shown by applying it to degraded AVIRIS data. The authors make comparisons with a more popular NDVI technique to show the advantage of our method.

1. Introduction

The Multiangle Imaging SpectroRadiometer (MISR) (Diner et al. 1989) is scheduled for launch in 1998 on the EOS-AM platform as part of the Earth Observing System (Dozier 1994). To improve the pointing accuracy of each MISR camera after launch, a series of image navigation techniques are planned, the details of which are described by Lewicki et al. (1994). Based solely on orbital parameters to locate camera position as a function of time, the error (one standard deviation) in the along track linear displacement at the surface is expected (Diner 1994, personal communication) to range from about 3 km for the nadir camera to 17 km for the most oblique (i.e., 70.5°) camera. Like other image navigation techniques (e.g., Emery et al. 1989), further improvements to camera positioning will be made by matching geographic points or features on the surface that are clearly visible in the camera image. For MISR, approximately 100 points per orbit will improve the pointing accuracy to better than 100 m at nadir (about 700 m at 70.5°).

Surface features must of course be identifiable through possible haze or cloud cover if they are to be usable for navigation purposes. When dealing with automated navigation (like that of MISR), it is thus desirable to improve the efficiency of feature searching by objectively excluding those cases with too much cloud obscuration. This requires the initial processing step of dividing pixels into "clear enough" and "cloudy" categories (the term "clear enough" is used because ground features can frequently be detected through thin cloud, so that the scenes do not have to be "clear" in a conventional sense).

This paper describes a masking technique that has been developed to objectively categorize radiometric data as "cloudy" or "clear enough" for image navigation purposes. While this is motivated and presented in the context of the MISR, the mask may be of general interest for similar use by other instruments. For brevity we call it the INCM (image navigation cloud mask) and note at the outset that it differs from conventional cloud masks in several ways. Since its primary function is as a screen that conservatively removes the most cloudy data from the subsequent navigation processing stream, it is not intended to be a useful determinant of cloud properties. It also tolerates the presence of thin cloud, since surface features may often be detected through thin cloud. Most importantly, however, it differs from conventional masks by being extremely tolerant of scene misidentification errors at land–water boundaries.

The MISR data will be the first of its kind, making comprehensive prelaunch testing of the INCM impossible, and operational thresholds may require resetting once data from the initial orbits become available. For now, we present results from interim tests using data collected by the Airborne Visible–Infrared Imaging Spectrometer (AVIRIS). Due to a somewhat restricted choice of available scenes, this testing is for nadir views with fairly high solar elevation only. As a guide to worse

Corresponding author address: Larry Di Girolamo, Department of Atmospheric and Oceanic Sciences, McGill University, 805 Sherbrooke Street West, Montreal, PQ H3A 2K6, Canada.

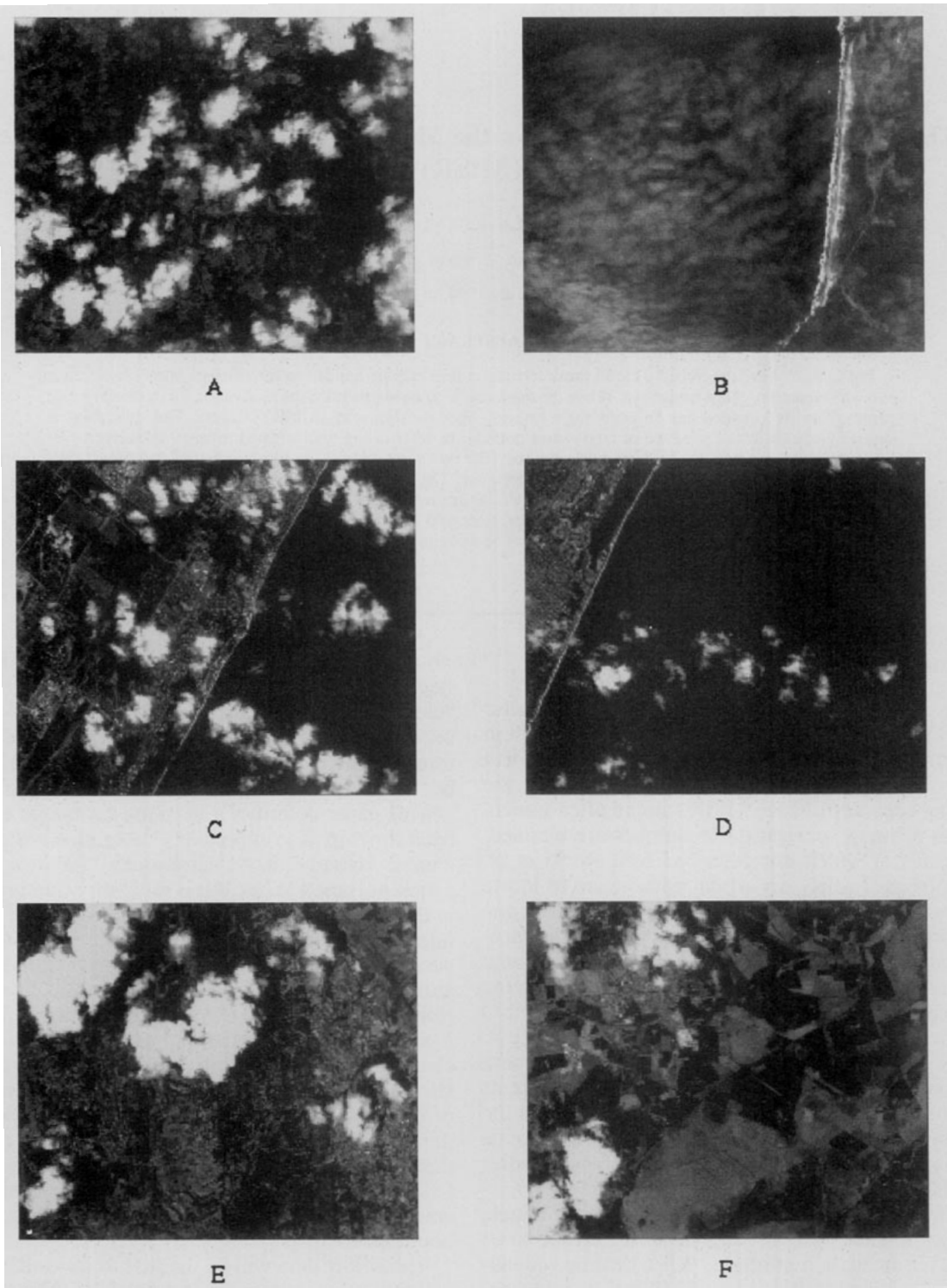

FIG. 1. Full-resolution 0.67-μm channel AVIRIS images listed in Table 1. The capital letter at the bottom of each image identifies the scene in Table 1. The saturation level of the linear gray scale has been lowered to augment surface details.

TABLE 1. AVIRIS scenes analyzed in this study. The first six digits of the scene ID gives the date (yy/mm/dd) the image was taken. Here μ_0 is the cosine of the solar zenith angle.

Scene	AVIRIS scene ID	Centered position	μ_0
A	910620A.R2.S2	43.61°N, 11.12°E	0.88
B	900814A.R9.S1	45.08°N, 123.97°W	0.82
C	921119B.R8.S12	26.17°N, 81.81°W	0.69
D	921119B.R8.S13	26.23°N, 81.86°W	0.69
E	910628B.R5.S4	43.68°N, 4.81°E	0.93
F	910628B.R6.S2	43.55°N, 4.86°E	0.93
G	900810A.R6.S4	36.60°N, 117.69°W	0.87
H	920603B.R17.S5	33.90°N, 115.86°W	0.89
I	921007B.R2.S3	37.94°N, 118.97°W	0.71
J	921007B.R4.S3	38.02°N, 119.03°W	0.72

case behavior, we also discuss the results obtained from model simulation for oblique view and oblique illumination.

Brief descriptions of the MISR instrument and the AVIRIS test-data are presented in section 2. Section 3 lists MISR's strict requirements of the image navigation cloud mask (INCM). In section 4 we derive the INCM algorithm, and in doing so we introduce a new two-channel (0.67 and 0.86 μm) observable that is better suited for cloud detection than either channel alone. Test results of the INCM algorithm are given in section 5, and in section 6 the INCM is compared to a typical approach to cloud masking for image navigation. Finally, section 7 summarizes the INCM performance.

2. Data

The Multiangle Imaging SpectroRadiometer (MISR) (Diner et al. 1989) will provide continuous multiangle coverage of the earth at nine discrete angles corresponding to viewing zenith angles at the surface of 0°, ±26.1°, ±45.6°, ±60°, and ±70.5°. This will be accomplished by four fixed cameras looking forward in the along-track direction, four looking aft, and one at nadir. Each off-nadir camera is designed to give a similar cross-track resolution of about 275 m and to provide images in a push-broom fashion in four spectral bands (443, 555, 670, 865 nm). The swath width will

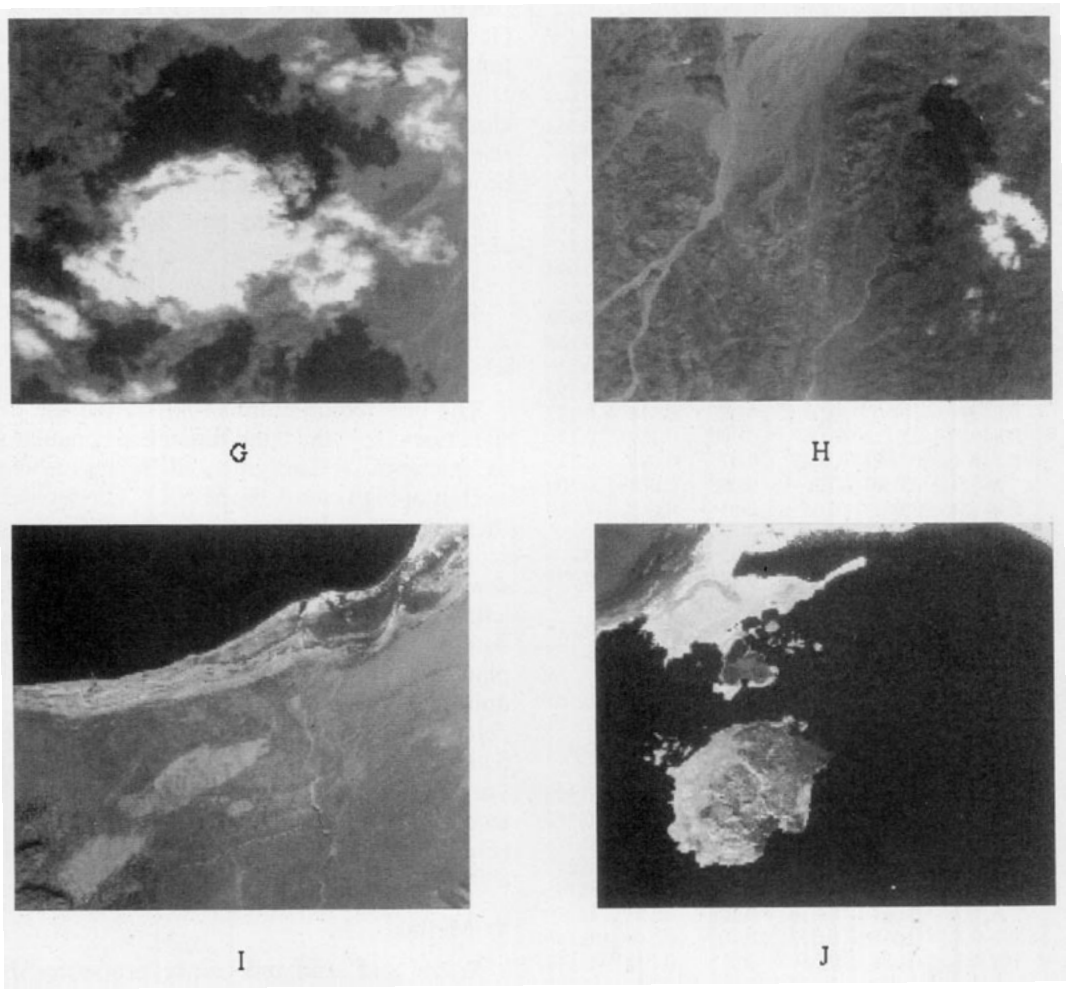

FIG. 1. (*Continued*)

TABLE 2. Tabulated values of the predetermined clear-sky thresholds (PCST). The values are binned according to the cosine of the solar zenith angle (μ_0) in intervals of 0.1 and the relative azimuth angle φ_r, between sun and view, in intervals of 30°. Each tabulated PCST value is the maximum PCST value that occurs within the bin interval.

		MISR camera angle				
φ_r	μ_0	0°	26.1°	45.6°	60°	70.5°
0°–30°	0.1–0.2	0.303	0.375	0.587	1.130	2.594
	0.2–0.3	0.212	0.266	0.423	0.852	1.789
	0.3–0.4	0.122	0.157	0.260	0.575	0.983
	0.4–0.5	0.079	0.102	0.176	0.425	0.632
	0.5–0.6	0.060	0.076	0.132	0.340	0.513
	0.6–0.7	0.061	0.075	0.124	0.250	0.364
	0.7–0.8	0.061	0.073	0.117	0.161	0.215
	0.8–0.9	0.056	0.075	0.098	0.111	0.152
	0.9–1.0	0.051	0.054	0.059	0.078	0.109
30°–60°	0.1–0.2	0.303	0.361	0.509	0.829	1.369
	0.2–0.3	0.212	0.256	0.368	0.610	1.014
	0.3–0.4	0.122	0.151	0.226	0.391	0.660
	0.4–0.5	0.079	0.099	0.150	0.266	0.447
	0.5–0.6	0.060	0.073	0.109	0.189	0.307
	0.6–0.7	0.061	0.071	0.098	0.157	0.243
	0.7–0.8	0.061	0.069	0.087	0.125	0.179
	0.8–0.9	0.056	0.063	0.072	0.098	0.137
	0.9–1.0	0.051	0.058	0.056	0.074	0.103
60°–90°	0.1–0.2	0.303	0.335	0.400	0.512	0.675
	0.2–0.3	0.212	0.237	0.289	0.382	0.514
	0.3–0.4	0.122	0.140	0.179	0.251	0.353
	0.4–0.5	0.079	0.092	0.121	0.177	0.257
	0.5–0.6	0.060	0.069	0.090	0.133	0.193
	0.6–0.7	0.061	0.067	0.083	0.123	0.173
	0.7–0.8	0.061	0.064	0.076	0.113	0.152
	0.8–0.9	0.056	0.057	0.065	0.085	0.115
	0.9–1.0	0.051	0.049	0.052	0.069	0.094
90°–120°	0.1–0.2	0.303	0.314	0.343	0.396	0.472
	0.2–0.3	0.212	0.223	0.249	0.296	0.364
	0.3–0.4	0.122	0.131	0.155	0.197	0.256
	0.4–0.5	0.079	0.087	0.107	0.142	0.193
	0.5–0.6	0.060	0.067	0.083	0.111	0.152
	0.6–0.7	0.061	0.067	0.080	0.102	0.135
	0.7–0.8	0.061	0.067	0.077	0.093	0.119
	0.8–0.9	0.056	0.061	0.068	0.081	0.104
	0.9–1.0	0.051	0.053	0.056	0.067	0.089
120°–150°	0.1–0.2	0.303	0.303	0.329	0.388	0.470
	0.2–0.3	0.212	0.216	0.245	0.299	0.373
	0.3–0.4	0.122	0.129	0.160	0.211	0.276
	0.4–0.5	0.079	0.089	0.118	0.162	0.216
	0.5–0.6	0.060	0.072	0.098	0.133	0.175
	0.6–0.7	0.061	0.073	0.094	0.121	0.154
	0.7–0.8	0.061	0.074	0.090	0.109	0.133
	0.8–0.9	0.056	0.068	0.079	0.092	0.111
	0.9–1.0	0.051	0.057	0.063	0.073	0.091
150°–180°	0.1–0.2	0.303	0.302	0.337	0.416	0.508
	0.2–0.3	0.212	0.216	0.254	0.324	0.411
	0.3–0.4	0.122	0.131	0.171	0.233	0.314
	0.4–0.5	0.079	0.091	0.130	0.184	0.247
	0.5–0.6	0.060	0.075	0.109	0.157	0.195
	0.6–0.7	0.061	0.076	0.106	0.138	0.170
	0.7–0.8	0.061	0.077	0.103	0.119	0.146
	0.8–0.9	0.056	0.069	0.082	0.100	0.119
	0.9–1.0	0.051	0.063	0.066	0.076	0.093

be about 360 km from an expected 705-km altitude, sun-synchronous orbit. This will provide complete global coverage in times ranging from 2 days at the poles to 9 days at the equator.

To test the cloud mask, data of similar spectral and spatial resolution as MISR are required. We have chosen data from AVIRIS, a complete description of which is given by Vane (1987). In short, AVIRIS has 224 spectral bands, approximately 10 nm in width, ranging from 0.4 to 2.5 μm—four of which are similar to MISR channels. The instrument is flown at an altitude of 20 km aboard an ER-2 aircraft and views only at nadir. This results in a swath width of 12 km with a pixel size of 20 m × 20 m. The cloud mask algorithm is tested on degraded AVIRIS data, where an array of 14 × 14 pixels is averaged to give a 280 m × 280 m spatial resolution. The AVIRIS scenes employed in this study are given in Table 1, with their corresponding 0.67-μm channel images shown in Fig. 1.

3. Image navigation cloud mask requirements

The first step in MISR's image navigation algorithm is cloud detection. Most cloud detection algorithms (for a review see Di Girolamo 1992; Rossow et al. 1989; Goodman and Henderson-Sellers 1988) are designed for a particular dataset with a particular task in mind. However, no existing technique can handle the strict cloud masking requirements set forth by the MISR science team at the early level at which data will be processed. These requirements are that the INCM:

1) be applied separately to each camera;
2) be computationally fast;
3) utilize no ancillary data; and
4) be able to detect clouds of τ_m and greater, where τ_m is the maximum cloud optical thickness through which image navigation is still possible.

The first requirement prohibits the use of angular signatures [e.g., the band-differenced angular signature technique of Di Girolamo and Davies (1994a) for detection of high clouds by MISR]. The second requirement demands a very simple algorithm, eliminating radiative transfer and statistical techniques (e.g., Rossow et al. 1985)—only direct threshold techniques are left. The third requirement does not allow us to use data from other instruments onboard the EOS-AM platform or other sources. Fortunately, the fourth requirement alleviates much of the difficulty involved in detecting thin clouds; however, τ_m will depend on the feature contrast sought by the image navigation analysis. Thus, MISR's INCM must rely on direct threshold techniques for each camera and use only MISR data (except for predefined datasets) but need not worry if thin clouds are not detected.

4. Method

Water and land reflectance properties differ substantially and require different thresholds to discrimi-

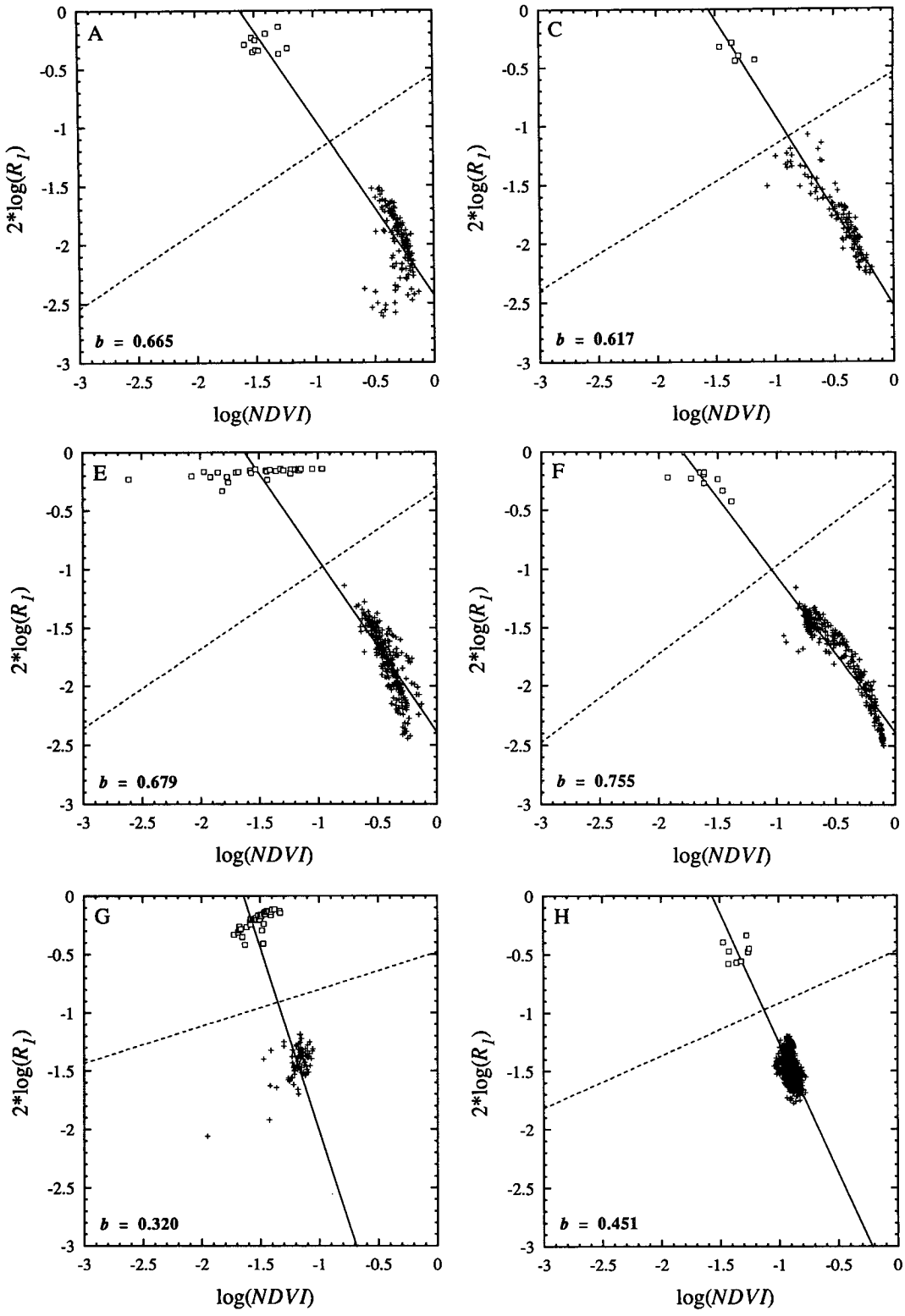

FIG. 2. Scatterplots of selected (see text) clear and cloudy regions for several degraded AVIRIS scenes chosen from Table 1. The capital letter at the top left corner of each scatterplot identifies the scene in Table 1. The squares correspond to completely cloudy pixels and the crosses correspond to completely clear pixels. The solid line passes through the sample averages of the clear and cloudy populations. The dashed line is perpendicular to the solid line and has the slope of b given at the bottom left corner of each scatterplot.

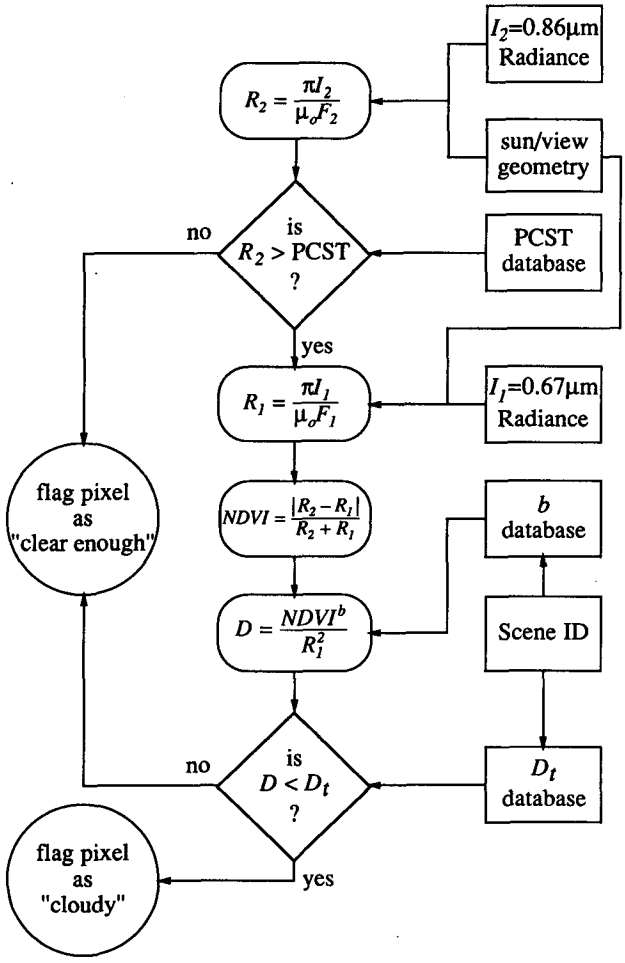

FIG. 3. A schematic diagram of MISR's image navigation cloud mask. Terms F_1 and F_2 are the 0.67- and 0.86-μm TOA incident flux, respectively.

nate between clear and cloudy sky over each surface type. Consequently, single thresholding masks can make large errors at land–water boundaries due to surface misclassification caused by pointing error—which can be large for prenavigated imagery. Yet these boundaries are the most useful features for image navigation!

Accordingly, we derive an INCM that is insensitive to land–water misclassification. Two different observables are generated for each pixel, one being sensitive to cloud over a water surface, the other to cloud over a land surface. As shown below, both observables must pass a threshold test for the pixel to be classified as "cloudy," whereas the "clear enough" classification can occur from a single test.

Let us consider a water observable W with a corresponding threshold W_t such that $W \geqslant W_t$ implies cloud. Similarly, let the land observable be L with a threshold L_t such that $L \leqslant L_t$ implies cloud. A simple thresholding algorithm that meets the cloud mask requirements is then:

if $W \geqslant W_t$ and $L \leqslant L_t$,

then "cloudy," otherwise "clear enough."

The choice for W and L is limited because of MISR's spectral coverage. The two most common observables that can be constructed from the MISR channels are a single-channel reflectance and a vegetation index. Vegetation indices, in particular the normalized differenced vegetation index (NDVI), have become popular in image navigation algorithms that distinguish land, water, and cloud (e.g., Bodes et al. 1992; O'Brien and Turner 1992). The NDVI is equal to $(R_2 - R_1)(R_2 + R_1)^{-1}$, where R_2 is the 0.86-μm channel top of atmosphere (TOA) reflectance, and R_1 is the 0.67-μm channel TOA reflectance. The values of NDVI are typically negative for clear-sky ocean, positive for clear-sky land, and close to zero for clouds. However, using NDVI alone can lead to misclassified pixels: rock and bare soil have NDVI ≈ 0, with negative values also being possible; snow and cloud shadows have NDVI < 0; and shallow waters having NDVI > 0 are common. As we will show in section 6, this can lead to problems in detecting inland features if NDVI is used for both W and L.

The shortcomings of using a single observable for both W and L led us to develop a two-observable technique for MISR's INCM. For W, the predetermined clear-sky threshold (PCST) given by Di Girolamo (1992) has been adopted. In short, the PCST is a simple 0.86-μm reflectance threshold for water surfaces that depends only on the viewing/solar geometry. MISR's 0.86-μm channel was chosen because its TOA measured radiance is less sensitive to changes in atmospheric and oceanic constituents than other MISR channels. The thresholds were derived using LOWTRAN 7 (Kneizys et al. 1988) coupled to an ocean surface model. The maximum clear-sky reflectance under various clear-sky–sea surface state scenarios defines the threshold. The conditions giving rise to maximum clear-sky reflectance were a flat ocean surface, sub-Arctic atmospheric profile, and high turbidity (no ocean whitecaps were taken into account; see section 5). The resultant thresholds can detect clouds that have visible optical depths greater than 0.5; thus, a conservative τ_m is inherently set by the PCSTs. The PCST values are given in Table 2.

For L, we have considered a particular combination of two MISR channels, namely

$$D = \frac{\mathrm{NDVI}^b}{R_1^2}, \tag{1}$$

where the exponent b is chosen to maximize the separation between clear and cloudy pixels.

To obtain b, we note that (1) can be rewritten as

$$2\log(R_1) = b\log(\mathrm{NDVI}) - \log(D). \quad (2)$$

Thus, a straight line on a $2\log(R_1)$ versus $\log(\mathrm{NDVI})$ graph has a slope of b and an intercept of $-\log(D)$. As examples, Fig. 2 shows scatterplots of selected regions from scenes A, C, E, F, G, and H in Fig. 1. These scenes were chosen because they contain clear and cloudy pixels that are easily discernible by eye, allowing a subjective choice of clear and cloudy pixels to be used in Fig. 2. In each of the six scatterplots, two distinct clusters are observed: pixels that are completely cloudy and pixels that are completely clear. The choice of b will depend on the nature of the cloud detection technique—that is, whether D is used in a direct thresholding technique or in a statistical technique. For example, Di Girolamo and Davies (1994b) have used a statistical technique—the spatial variability index (Brest and Rossow 1992) of D (DSVI)—for cloud detection. For this method, principal component analysis (Preisendorfer 1988) was applied to the clear-sky pixels in order to obtain b. The philosophy was to choose the value of b that maximizes the variability in D amongst the clear-sky population. Thus, b takes on the slope of the principal axis of maximum variance. Using three full-resolution AVIRIS scenes (vegetated surfaces), an average b of 0.6 was obtained. This made cloud detection simple since DSVI is very large over clear skies compared to cloudy skies.

For MISR's INCM, only a direct thresholding technique (applied on a pixel-by-pixel basis) is possible. For this method, b is taken as the slope of the line that is orthogonal to the line connecting the sample averages of the clear and cloudy populations, as depicted in Fig. 2. This leads to a maximum separation of clear and cloudy D values and a much larger dynamic range of D compared to R_1 or NDVI alone. Our choice of b is given on the individual scatterplots of Figure 2. Here b ranges from 0.32 to 0.755, with higher values having denser vegetation cover. This small range in b suggests that b can be coarsely divided into scene type (e.g., dry versus vegetation), with only a small effect on the optimum cloud discriminability of D.

A schematic of the INCM is shown in Fig. 3. Note that we use the absolute value of the NDVI in calculating D because D is not defined for $\mathrm{NDVI} \leq 0$ [cf. (1)]. As discussed earlier, negative NDVIs are common over cloud-free ocean and can also occur over cloud-free land. Taking the absolute value of the NDVI in calculating D works to our advantage: clear sky over ocean should pass the PCST test, at which point the D_t test is not performed; if the PCST test does fail for clear ocean pixels, perhaps due to oceanic whitecaps, the D_t test may still classify the pixels as "clear enough," provided the $|\mathrm{NDVI}|$ is sufficiently large. The same reasoning applies to land surfaces that have $\mathrm{NDVI} < 0$.

5. INCM test results

Before image navigation and geometric calibration takes place, rough estimates of the pointing knowledge of each MISR camera will be known with an uncertainty that depends on the camera view angle. The expected range in pointing uncertainty (in terms of the along-track linear displacement at the surface) ranges from about 3 km at nadir to 17 km for the most oblique camera (Diner 1994, personal communication). Therefore, it will be possible for the D thresholds to be georeferenced and classified by scene type, albeit at a degraded resolution comparable to the pointing uncertainty. For this study, we have used the WE1.4D version of Olson's global ecosystem database (NOAA-EPA Global Ecosystems Database Project 1992) to define our scene type. This database contains 59 ecosystem classes mapped onto a 10-min grid over the globe. Because of the limited amount of AVIRIS data available to us, AVIRIS training scenes are used to derive the D_t to be used on the AVIRIS test scenes. Term D_t was set to the minimum D value (of positive NDVI) of the clear-sky portion of the training scene. The derived D_t of a training scene is applied to a test scene that has the same ecosystem type and similar sun angle. Scenes A and B are an exception, having been classified with different ecosystems. However, both are vegetated, differing slightly in vegetation type. Also, scenes I and J have their ecosystem type misclassified by our database as "snowy non-Boreal conifer forest." According to the U.S. Geological Survey (1985, 1988), the region is more like dry highland with a substantial amount of inland water (Mono Lake). Table 3 lists the training scenes, the b and D_t values (and NDVI_t used in section 6), and the corresponding test scene. The training and test scene must use the same b value so that the D_t derived in the training scene is applicable. For scenes E and F, b is equal to the average b value calculated for scenes E and F given in Fig. 2. Similarly for scenes G and H, b is equal to the average b value calculated for scenes G and H. The b value for scenes I and J is taken as the b value of scenes G and H because of the similar scene types. Scenes A–B and C–D use the b value calculated for scenes A and C, respectively.

TABLE 3. AVIRIS training and test scenes with their corresponding b, D_t, and NDVI_t values.

Training scene	b	D_t	NDVI_t	Test scene
A	0.67	8.5	0.0229	B
C	0.62	4.2	0.0862	D
E	0.72	3.7	0.166	F
G	0.39	4.2	0.0443	H
I	0.39	0.98	0.0011	J

As is often the case, the success of a cloud mask is difficult, if not impossible, to ascertain quantitatively due to the lack of a "truth" dataset (e.g., Rossow et al. 1985). Intercomparison with other cloud detection algorithms requires that they share the same goal and definition of what constitutes a cloud. In our situation, the "truth" against which a quan-

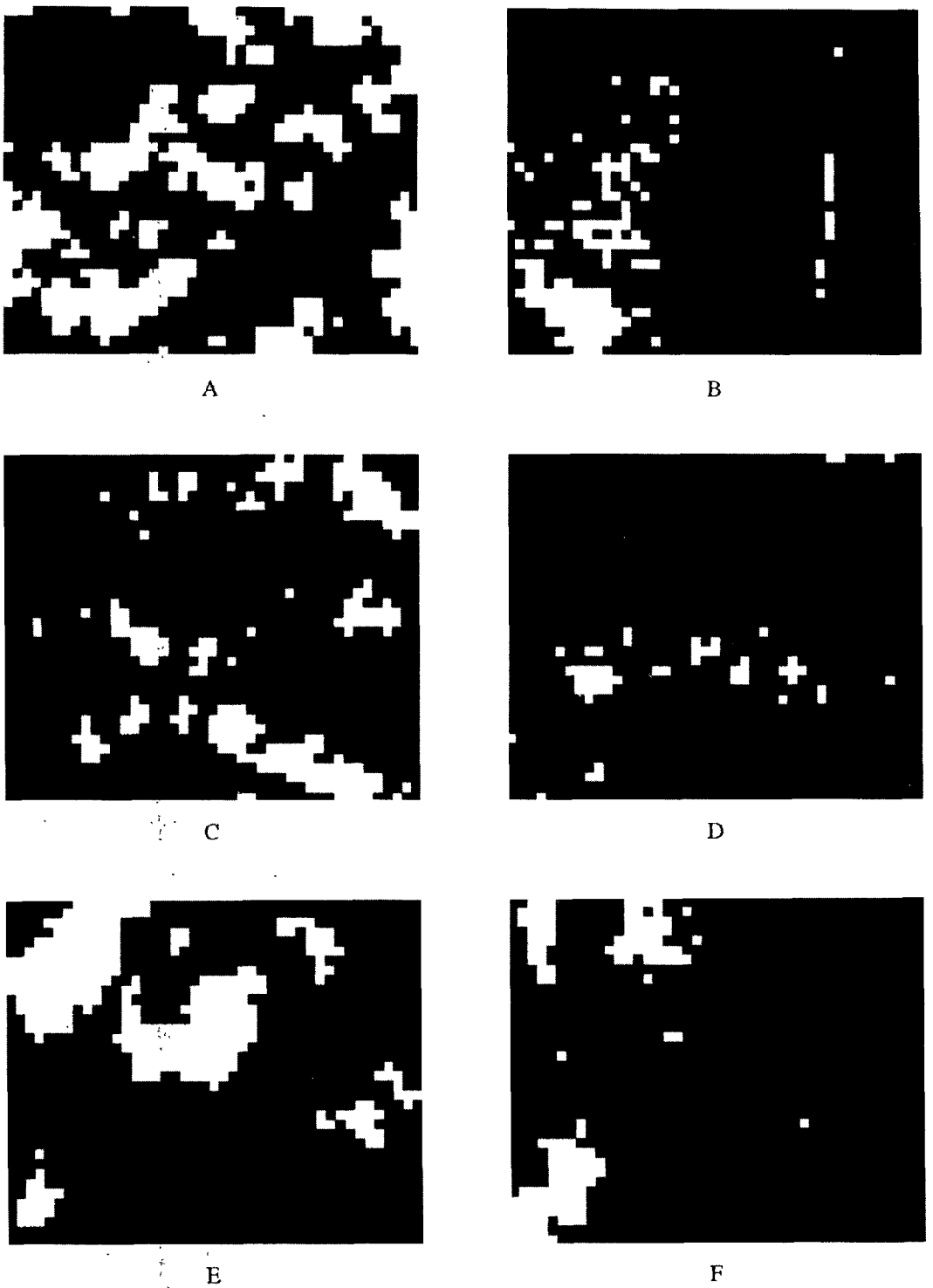

FIG. 4. Output of the INCM applied to the degraded AVIRIS scenes listed in Table 1. The letter under each image identifies the scene in Table 1. The white and black areas represent "cloudy" and "clear enough" pixels, respectively.

titative test of success might be made would inevitably be derived from a subjective dataset. Accordingly, we make only a qualitative assessment of the INCM success by subjectively comparing the original images with the mask results. For the scenes presented, subjective assessment of cloud presence, as

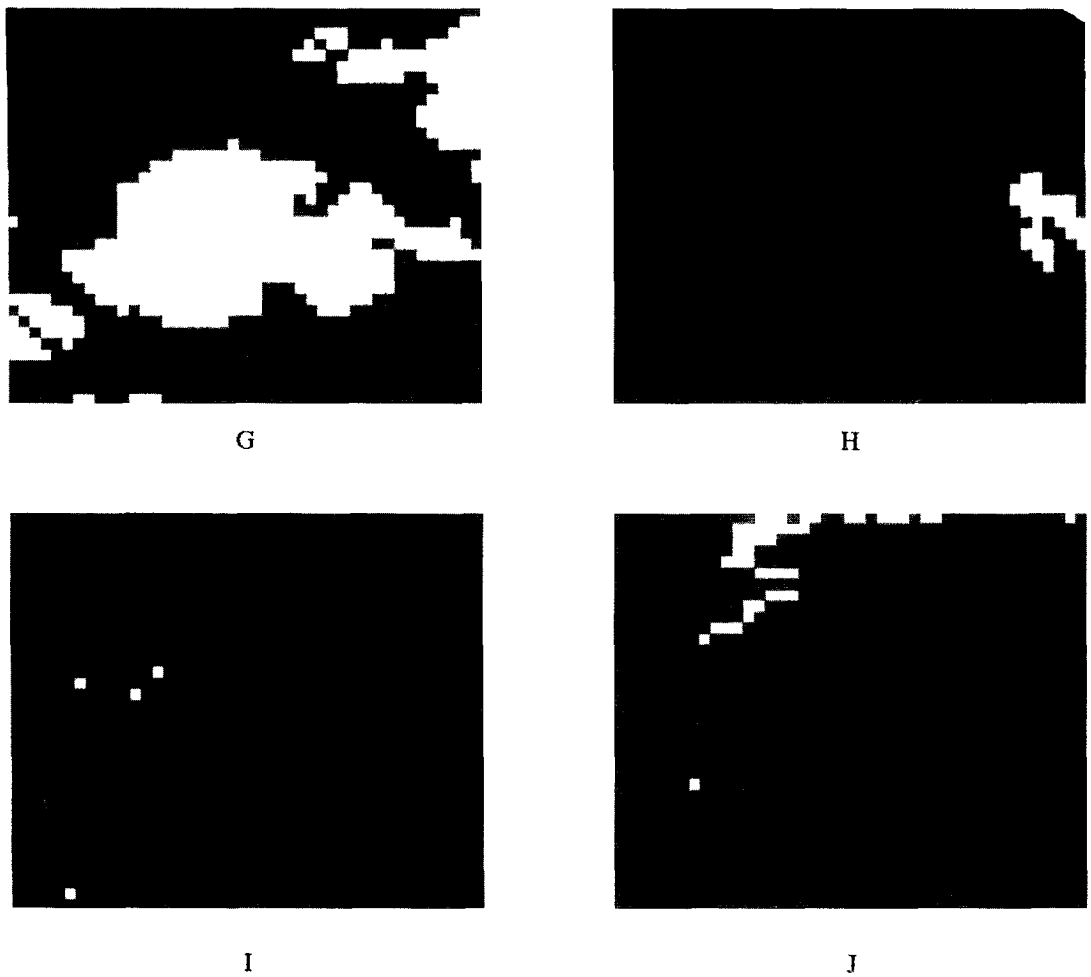

FIG. 4. (*Continued*)

well as of surface features detectable through thin cloud, can be made with little ambiguity.

The output of the INCM for each scene listed in Table 3 is shown in Fig. 4. By comparing the images of Fig. 4 with the corresponding high-resolution images of Fig. 1, we see that the INCM performs quite well for all scenes. However, there are some special notes to be made.

1) Scene B is interesting in that a thin layer of cloud covers most of the scene, so that only the thicker portions of the cloud are detected as "cloudy." For the thinner parts of the cloud, the INCM has labeled these regions "clear enough." This is desirable since we see that in the presence of such thin clouds, image navigation can still take place. We also note that some of the white breaking water along the coast has been labeled as "cloudy." In fact, more ocean pixels have been labeled as "cloudy" by the PCST test (an indication of its conservative nature). However, many of these pixels had NDVIs large enough to pass the D test—highlighting the benefit in taking |NDVI| in calculating D.

2) For scene F, we note there are two pixels classified as "cloudy" that, according to Fig. 1, appear to be clear. This simply indicates the shortcoming of using a coarse-resolution scene classifier. Also, a small lake exists in the lower-right corner of Fig. 1F. The 0.86-μm reflectance is slightly larger than the PCST; thus, it fails the PCST test. Fortunately, with the NDVI sufficiently negative and R_1 low, the lake-pixels pass the D_t test.

3) For scene G, the large shadow region (see Fig. 1) has correctly been classified as "clear enough." The shadow region contains many pixels with NDVI < 0. Because the absolute value of the NDVI is taken and the 0.67-μm reflectances are low, the D values are large within the shadow region, which is correctly classified.

4) For scenes I and J, the pixels that have been classified as "cloudy" are pixels over land that have D values very close to zero. However, roughly 20% of the land pixels have NDVI < 0, many of which have passed the D_t test.

Unfortunately, the limited amount of test data places certain bounds on the generality of our test

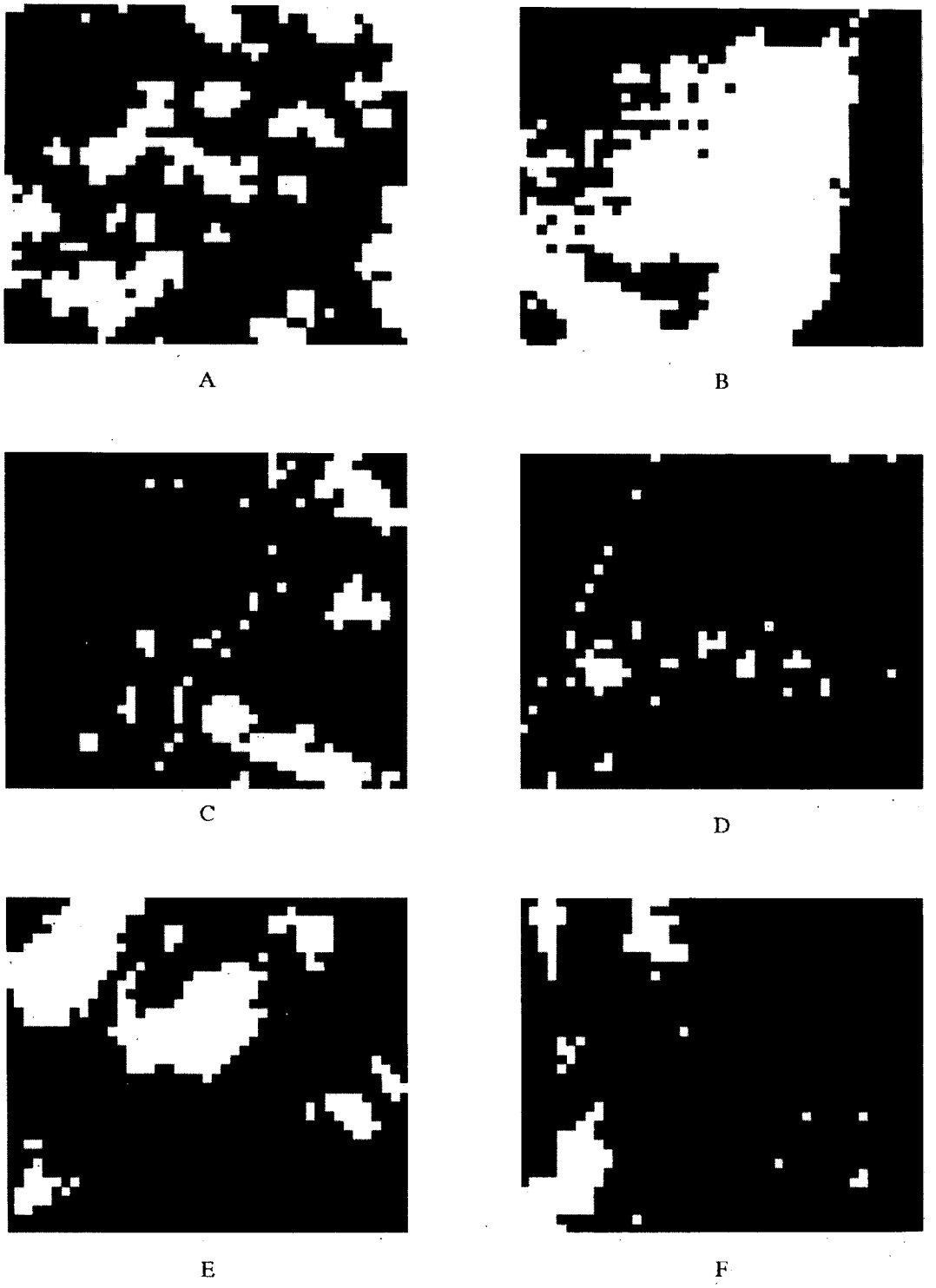

FIG. 5. Output of the NCM applied to the degraded AVIRIS scenes listed in Table 1. The letter under each image identifies the scene in Table 1. The white and black areas represent "cloudy" and "clear enough" pixels, respectively.

results to other scenes, because only a limited range in ecosystem type and sun–view geometry have been examined. Surfaces, such as sand or snow, that exhibit values of NDVI ≈ 0 are expected to cause problems for D to discriminate clear from cloudy (the INCM will classify such land surfaces as cloudy).

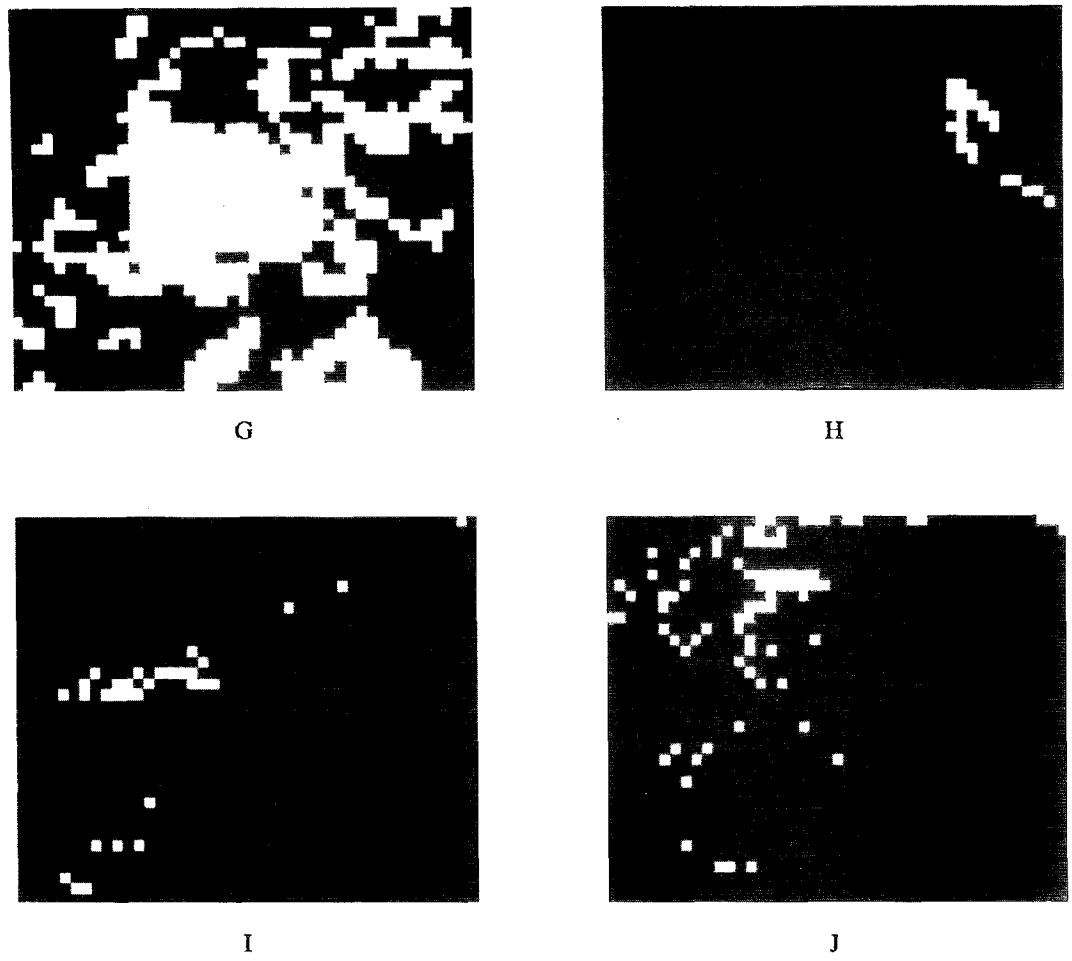

FIG. 5. (*Continued*)

However, it is unlikely that deserts of sand and snow will be useful for navigating MISR imagery. Of greater concern is our narrow test coverage in sun–view geometry. The AVIRIS instrument is nadir-pointing and tends to fly at a couple of hours on either side of local noon. MISR, on the other hand, will have a wide range of sun–view geometries. Both D_t and b are expected to vary with sun and view, the extent of which is the subject of ongoing research; however, for a particular b value, we can simulate how D varies with sun and view and infer its effect on clear–cloud discrimination.

We used LOWTRAN 7 (Kneizys et al. 1988) to simulate MISR measurements over a variety of sun–view geometries and clear-sky atmospheric conditions. A Lambertian surface was used with typical surface albedo values. (Naturally, the Lambertian assumption may not hold; however, the general trend in D with sun–view geometry is expected to remain.) We found that D decreases with increasing solar zenith angle and increasing view angle. The rate of decrease in D also depends on the relative azimuth angle. The largest decrease occurs for observations at 0° (forward scatter) and to a lesser extent at 180°. The minimum decrease is at 90°/270°. As atmospheric turbidity increases, D changes more rapidly with sun–view geometry.

This does not infer that clear–cloud discrimination is impossible when observations are taken at oblique view angles under low sun illumination. What it does indicate is that clear–cloud discrimination becomes more difficult because the amount of signal that can be used to set thresholds has been reduced; the degree of difficulty can only be ascertained with the availability of data. However, it appears that sufficiently large signal in D remains for the INCM to function properly over a wide range of sun–view geometries.

6. Intercomparison

We can compare the above INCM against a similar algorithm that uses the NDVI for both W and L. The NDVI water threshold is set at −0.02 in accordance

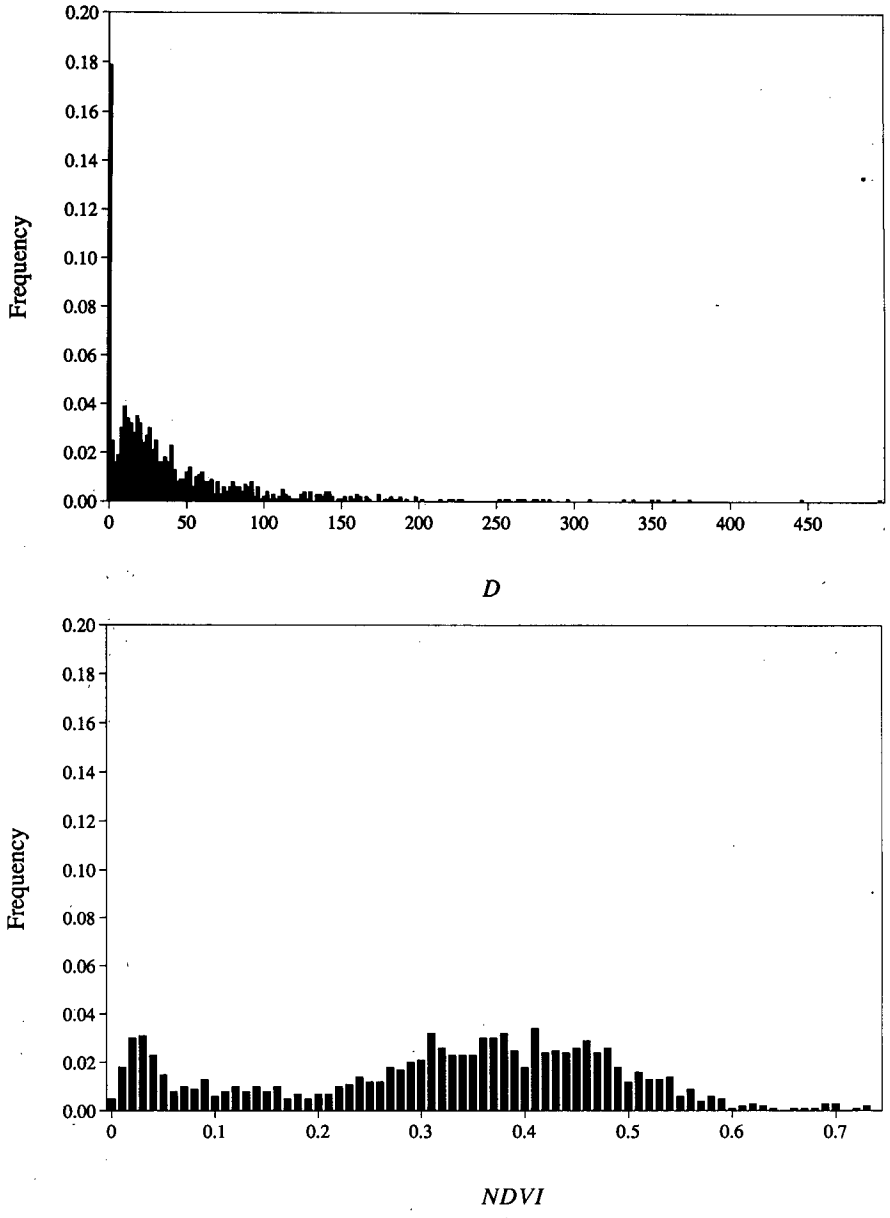

FIG. 6. Frequency histograms of (a) D, binned at equal intervals of 2, and (b) NDVI, binned at equal intervals of 0.01. The data is taken from scene E.

with O'Brien and Turner (1992). Over land, the NDVI was set to the minimum positive NDVI value of the clear-sky portion of the training scene. Table 3 lists the land $NDVI_t$ with their corresponding training and test scenes.

The output of the $NDVI_t$ cloud mask (NCM) for each scene listed in Table 3 is shown in Fig. 5. By comparing Fig. 5 with Figs. 1 and 4, the following observations are made for each scene.

Scene A: Only small differences are observed between the INCM and NCM. The small differences, however, favor the INCM.

Scene B: Large differences exist between the INCM and the NCM outputs. Many more pixels have been labeled as "cloudy" by the NCM over much of the ocean and coastline, as compared to the INCM, due to the thin cloud that occurs over most of the scene. However, this scene does appear to be useful for image navigation since the coastline is easily recognizable. Thus, the INCM output is the preferred choice for this scene.

Scene C: The NCM performs poorly; many of the inland clouds, detected by the INCM, have not been detected by the NCM. Also several clear-sky–coastline pixels have been misclassified as "cloudy" by the NCM.

Scene D: Many clear-sky–coastline pixels are misclassified as "cloudy" by the NCM.

Scene E: The NCM has classified more pixels as "cloudy" compared to the INCM. This is because many of the cloud-shadow pixels have been misclassified by the NCM as "cloudy."

Scene F: The two pixels that have been misclassified as "cloudy" by the INCM have also been misclassified by the NCM, along with several other pixels. Also, the clouds at the top of the image have been slightly underestimated by the NCM.

Scene G: The NCM performs poorly for this scene. Most of the cloud shadows are classified as "cloudy," where the INCM correctly classifies them as "clear enough." Also, the INCM and NCM differ in the amount of cloud surrounding the large central cloud in the image.

Scene H: The NCM has classified the cloud shadow as "cloudy"—but has missed most of the cloud itself!

Scene I and J: Most of the NCM-misclassified pixels are coastline pixels.

Our largest concern is the misclassification of clear-sky–coastline pixels. Since coastlines are popular features to extract for image navigation, it is mandatory that these pixels are properly classified as "clear enough" or "cloudy." From the above intercomparison, the INCM is clearly superior to the NCM in this respect and in providing a cloud mask that is closer to the true cloud cover.

As a final note, Fig. 6 shows histograms for D and NDVI over scene E and is typical for vegetated scenes. The frequency distribution of D and NDVI are very different. Note that for D most cloudy pixels reside within the first bin. Based on Fig. 6, we can guess that $2 < D_t < 8$ and $0.06 < \mathrm{NDVI}_t < 0.21$. Within this range lies about 6% of the D pixels and 13% of the NDVI pixels, indicating the ability of D to provide better separation between clear and cloudy pixels.

7. Summary

We have developed a technique for the image navigation cloud mask (INCM) of the forthcoming Multiangle Imaging Spectroradiometer (MISR). The purpose of the INCM is to classify pixels for image navigation analysis as either "clear enough" or "cloudy." This will lead to a more efficient selection criterion of clear scenes for image navigation of MISR imagery. The INCM employs a simple two-step direct threshold technique, applied to the observables R_2 and D, designed to detect clouds in the presence of land–water boundaries as well as to meet the requirements listed in section 3. The introduction of the observable D allows us to improve the cloud detectability contained in the 0.86- and 0.67-μm MISR channels in a simple, straightforward fashion. This was shown in section 6 by making comparisons with an NDVI approach to cloud detection.

Application of the INCM to certain scenes revealed that breaking water along coastlines may be misclassified as "cloudy" due to the NDVI being very close to zero. In fact, it can be generally stated that pixels with 0.86-μm reflectance greater than the PCST, and with NDVI ≈ 0, will always be classified as "cloudy." The misclassified "cloudy" pixels of scene I and J meet this criteria. This would also extend to other surfaces, such as snow cover, for which we had no high-resolution data. Thus, the INCM has limitations that depend on the spectral signature of the underlying surface. Another limitation lies in the derivation of the PCST where no reflected radiation off the basin's floor was taken into account. This may become important for measurements over shallow water. Finally, modeled results for the sun–view variability of D suggest that difficulties may exist in clear–cloud discrimination at large viewing and solar zenith angles. Note, however, that these limitations lead to a conservative cloud mask—which is preferable. For instance, MISR's image navigation algorithm will employ a search window over which a particular land feature is sought. If the INCM reveals a cloud fraction greater than 10% within the search window, the land feature is rejected. So, inherent in the INCM is a certain amount of tolerance for clear pixels to be misclassified as cloudy.

Unfortunately, not all ecosystem types and sun–view geometries could be tested with the limited amount of AVIRIS data available to us. Moreover, the b and D_t values given in Table 3 are not necessarily those that will be used by MISR; they are for INCM testing purposes only. Therefore, the results of the INCM presented here must only be considered as preliminary (although the optimum cloud discriminability of D remains—regardless of the sun–view geometry and ecosystem type). Efforts will continue up to launch time to develop a prelaunch dataset of b and D_t that are a function of the sun–view geometry and ecosystem type. A few months after launch, the dataset of b and D_t will continually be updated based on MISR measurements and postnavigation data processing (Diner et al. 1994).

As a final note, we emphasize that the cloud mask presented in this paper is intended for image navigation purposes only. As such, the cloud mask can tolerate errors in classification since no geophysical parameters (i.e., cloud, aerosol, and surface properties) are derived on the basis of the INCM classification. The derivation of such geophysical parameters for MISR are made at a later stage of data processing and will employ a much more sophisticated cloud detection scheme, including the use of DSVI (Diner et al. 1994).

Acknowledgments. We would like to thank Lisa Ramsaran for her aid in the preparation of the cloud mask code, and Eric Danielson and Brian Rheingans for the distribution of the AVIRIS data. Partial support from the Jet Propulsion Laboratory of the California Institute of Technology under Contract 959085 and

from the Natural Sciences and Engineering Council of Canada is gratefully acknowledged.

REFERENCES

Bodes, P., P. Brunel, and A. Marsouin, 1992: Automatic adjustment of AVHRR navigation. *J. Atmos. Oceanic Technol.*, **9,** 15–27.

Brest, C. L., and W. B. Rossow, 1992: Radiometric calibration and monitoring of NOAA AVHRR data for ISCCP. *Int. J. Remote Sens.*, **13,** 235–273.

Di Girolamo, L., 1992: On the detection of cirrus clouds from satellite measurements. Center for Climate and Global Change Research, Report No. 92-8, McGill University, 67 pp.

——, and R. Davies, 1994a: A band-difference angular signature technique for cirrus cloud detection. *IEEE Trans. Geosci. Remote Sens.*, **32,** 890–896.

——, and ——, 1994b: Optimizing the use of the 0.67 μm and 0.86 μm radiometric data for cloud detection. *Eighth AMS Conf. on Atmospheric Radiation,* Nashville, TN, Amer. Meteor. Soc., 466–467.

Diner, D. J., and Coauthors, 1989: MISR: A Multi-angle Imaging SpectroRadiometer for geophysical and climatological research for EOS. *IEEE Trans. Geosci. Remote Sens.*, GE-**27,** 200–214.

——, E. Clothiaux, J. E. Conel, R. Davies, L. Di Girolamo, J.-P. Muller, T. Varnai, and D. Wenkert, 1994: Multi-angle Imaging SpectroRadiometer—level 2 algorithm theoretical basis: Top-of-atmosphere/cloud product. JPL D-11399, Jet Propulsion Laboratory, Pasadena, CA, 77 pp.

Dozier, J., 1994: Planned EOS observations of land, ocean and atmosphere. *Atmos. Res.*, **31,** 329–348.

Emery, W. J., J. Brown, and Z. P. Nowak, 1989: AVHRR image navigation: Summary and review. *Photogramm. Eng. Remote Sens.*, **55,** 1175–1183.

Goodman, A. H., and A. Henderson-Sellers, 1988: Cloud detection analysis: A review of recent progress. *Atmos. Res.*, **21,** 203–228.

Kneizys, F. X., E. P. Shettle, L. W. Abreu, J. H. Chetwynd, G. P. Anderson, W. O. Gallery, J. E. A. Selby, and S. A. Clough, 1988: Users guide to LOWTRAN 7. AFGL-TR-88-0177, 137 pp.

Lewicki, S. A., V. M. Jovanovic, M. M. Smyth, and K. L. Jones, 1994: Multi-angle Imaging SpectroRadiometer—level 1B2 algorithm theoretical basis: Geometrically-projected product. JPL D-11532, Jet Propulsion Laboratory, Pasadena, CA, 66 pp.

NOAA-EPA Global Ecosystems Database Project, 1992: *Global Ecosystems Database Version 1.0. User's Guide,* Documentation, Reprints, and Digital Data on CD-ROM. U.S. DOC/NOAA National Geophysical Data Center, Boulder, CO, 36 pp.

O'Brien, D. M., and P. J. Turner, 1992: Navigation of coastal AVHRR images. *Int. J. Remote Sens.*, **13,** 509–514.

Preisendorfer, R. W., 1988: *Principal Component Analysis in Meteorology and Oceanography.* Elsevier, 425 pp.

Rossow, W. B., 1989: Measuring cloud properties from space: A review. *J. Climate,* **2,** 201–213.

——, and Coauthors, 1985: ISCCP cloud algorithm intercomparison. *J. Climate Appl. Meteor.*, **24,** 877–903.

U.S. Geological Survey, 1985: 1: 100 000-scale metric topographic map, 38119-A1-TM-100. U.S. Geological Survey, Denver, CO.

——, 1988: 1: 100 000-scale metric topographic map, 37118-A1-TM-100. U.S. Geological Survey, Denver, CO.

Vane, G., (Ed.), 1987: Airborne Visible/Infrared Imaging Spectrometer (AVIRIS). JPL Publ., **87-38,** 73–87.